Leakage detection applied to the Da Hedong Reservoir dam (China) based on the flow-field fitting method

Xiang Zhao, Hongbing Zhang, André Revil, Yandong Liu, Fanxin Zeng, Ping Wang, Quan Ren

To cite this version:

Xiang Zhao, Hongbing Zhang, André Revil, Yandong Liu, Fanxin Zeng, et al.. Leakage detection applied to the Da Hedong Reservoir dam (China) based on the flow-field fitting method. Geophysics, 2024, 89, pp.KS105 - KS118. 10.1190/geo2023-0288.1 . hal-04729099

GEOPHYSICS, VOL. 89, NO. 4 (JULY-AUGUST 2024); P. KS105–KS118, 15 FIGS., 2 TABLES.
10.1190/GEO2023-0288.1

Leakage detection applied to the Da Hedong Reservoir dam (China) based on the flow-field fitting method

Xiang Zhao[1], Hongbing Zhang[2], André Revil[3], Yandong Liu[4], Fanxin Zeng[2], Ping Wang[2], and Quan Ren[2]

ABSTRACT

Detecting leakage in concrete gravity dams presents a formidable challenge. The flow-field fitting (FFF) method is used to identify leaks in China's Da Hedong Reservoir dam. We develop vertical- and horizontal-gradient approaches based on the transmitted signal electrical field. A plastic frame is developed to allow the probe to measure horizontal gradients. We determine the exact location of leaks at the reservoir's bottom and upstream face, respectively, assuming that current leakages are located in hydraulic leakage zones. Numerical experiments and water pressure tests reveal that the conductive silt layer beneath the reservoir can lower the response of the potential values at the leakage inlet, and the effect of the silt layer should be considered and not ignored when interpreting measured data. In addition, with regard to the principle of superposition, the contribution associated with metal pipes in the dam body can be roughly determined by subtracting it from the original potential field data, thereby aiding in locating leaks around the metal pipes. In addition, the FFF measurements from the reservoir's bottom also confirm the position of existing faults in the substratum at the reservoir site. Last, the results of the FFF method are tested against supporting evidence, such as ground penetrating radar and water pressure tests. In conclusion, these independent data confirm the effectiveness of the FFF method for leakage localization in the concrete gravity dam.

INTRODUCTION

Concrete gravity dams play a vital role in modern societies because they are used to store precious freshwater resources and provide residents with domestic water, irrigation water, and industrial water (Zeidan, 2015). Regular inspections of the dams are organized to prevent water losses, decrease the risk of failures, and protect water resources. In the dam, leakages can occur in the body of the dam, in the dam abutments, or in its foundations (Zhang et al., 2009; Gutierrez et al., 2015). In earth dams, it is well established that internal erosion and suffusion may cause dam failure (Foster et al., 2011; Ferdos et al., 2018). Early leakage detection associated with the level of leakage and pathways in the dam is therefore an important task to prevent water loss and failure of the structure (Peyras et al., 2011).

In leakage detection, geotechnical techniques have limitations in terms of cost-effectiveness and disturbance to the dams themselves (Cardarelli et al., 2014). Geophysical investigations are currently playing a great role in localizing leakages in dams and embankments due to the possibility of quickly and nonintrusively imaging their internal structure (e.g., Ikard et al., 2015). Different geophysical methods have been applied to detect leakages, such as electrical resistivity imaging (Sjödahl et al., 2006; Cho and Yeom, 2007), ground penetrating radar (GPR) (Slob et al., 2010), the self-potential method (Haas et al., 2013; Guo et al., 2022), the induced polarization method (Abdulsamad et al., 2019), the magnetometric resistivity method (Jessop et al., 2018), the mise-à-la-masse method (Ling et al., 2019a, 2019b), temperature measurements (Nan et al., 2022), and fluorescent tracer tests (Robert et al., 2012; Huang et al., 2018).

Manuscript received by the Editor 23 May 2023; revised manuscript received 10 March 2024; published ahead of production 13 April 2024; published online 5 June 2024.

[1]Hohai University, College of Earth Science and Engineering, Nanjing, China and Université Grenoble Alpes, Université Savoie Mont-Blanc, CNRS, EDYTEM, Bourget du Lac, France. E-mail: zhaoxiang1109@hhu.edu.cn
[2]Hohai University, College of Earth Science and Engineering, Nanjing, China. E-mail: hbzhang@hhu.edu.cn (corresponding author); 710744236@qq.com; pingwang@hhu.edu.cn; renquanlogo@163.com.
[3]Université Grenoble Alpes, Université Savoie Mont-Blanc, CNRS, EDYTEM, Bourget du Lac, France. E-mail: andre.revil@univ-smb.fr.
[4]Qingdao Water Conservancy Survey and Design Institute Co. Ltd, Qingdao, China. E-mail: 1825819700@qq.com.

Concrete gravity dams are the focus of the present work. This type of dam is usually characterized by a high dam height (typically >30 m) and can support large reservoir sizes. Furthermore, the upstream and downstream surfaces are typically vertical. The previous geophysical methods are more difficult to conduct from the concrete dam's surface (crest, upstream, and downstream faces). They are usually insufficient to detect leakages in such dams, particularly at the dam foundation and lower dam body. In addition, measuring the water seepage fields caused by leakage is also challenging. Therefore, it is necessary to find new strategies for locating leakages quickly and accurately. We chose the flow-field fitting (FFF) method (Dai et al., 2017; Zhao et al., 2023) to detect such leakages.

The FFF method leverages similarities between seepage and current fields in applicable conditions (He, 2018). In concrete gravity dams, water concentration along leakage pathways, which is conductive compared with the surrounding resistive concrete, facilitates detection by placing a sensor in the water near a potential leakage inlet. This avoids the need for detectors on the dam structure, reducing interference from structural nonuniformities. The FFF method, similar to the mise-à-la-masse technique in China, except for the power supply current selection and measurement (He, 2018; Ling et al., 2019a, 2019b), is also a noninvasive approach for detecting and locating water reservoir leaks. Inspired by the mise-à-la-masse method (Ketola, 1972; Mansinha and Mwenifumbo, 1983; Kumar et al., 2003), the FFF method injects an electrical current signal between two electrodes to measure the distribution of the transmitted signal electric field (two current electrodes A and B connected to a current generator and electrodes M and N are the voltage electrodes connected to a voltmeter). This enables the probe to access the leakage inlet and remain unaffected by the anisotropy of water conductivity. When the electrical and hydraulic leakages share paths, the contour map of the voltage difference can reveal information on leakage inlets and even leakage pathways. Effective for detecting dam leakages at the reservoir dam's bottom, upstream face, and even boreholes (e.g., Tingzhe et al., 2013; He, 2018; Zhao et al., 2021), the FFF method has played a significant role in China (Dai et al., 2017; Meng et al., 2019; Zhao et al., 2023). However, its application beyond China remains limited, prompting the need for further investigation.

In this paper, we first present the geologic site setting and the main structural characteristics of the concrete gravity dam. Then, we further extend the theory of the FFF method for analyzing potential leakage in a concrete gravity dam. The dam models are then developed and simulated with COMSOL Multiphysics (COMSOL Multiphysics Users' Guide, 2017) to demonstrate the effectiveness of the FFF technique in conducting field measurements. The simulation results provide a clear design for a field survey. Moreover, we devise a plastic frame that allows the probe to make horizontal gradient measurements (electrodes M and N arranged horizontally) at the upstream face in the field, in addition to the traditional vertical gradient method (electrodes M and N placed vertically). Finally, we corroborate the FFF technique through GPR scanning at the downstream face of the dam, borehole water pressure tests, and 3D FFF measurements in the field. Leaks are discovered at the dam foundation, the right shoulder, and around the metal pipes, especially in the middle of the dam and near the upstream mental pipe inlets.

FIELD SITE AND DAM DESCRIPTION

This section primarily focuses on describing the geologic context of the region encompassing the Da Hedong dam. Furthermore, a brief overview of the concrete gravity dam's geometry and structural aspects is presented.

Geologic settings

The Da Hedong Reservoir, located in the Laoshan district of Qingdao City, China, near the Yellow Sea, has three groups of tectonic faults developed under the control and influence of regional structures. These faults have predominant strikes ranging from northeast 10° to northeast 20°, northeast 55° to northeast 60°, and northwest 320° to northwest 340°, respectively, with dip angles close to vertical. The dam foundation is composed of medium- and coarse-grained granite, and several faults developed in the dam site and reservoir area. The majority of these faults are filled with lamprophyre veins (the lamprophyre has obvious softening effects when encountering water), while some are joint-dense areas and cataclastic rock belts, as shown in Figure 1.

Dam descriptions

The dam, constructed in 1997, is a gravity dam made of concrete and stone masonry. The dam is 424.0 m long, has a crest elevation of 86.5 m, and has a maximum height of 65.0 m. The upstream and downstream faces are vertical above the 82.0 m elevation. A 1.0 m thick cut-off wall of C20 concrete serves as the foundation below the 60.0 m elevation, whereas a 1.0 m thick cement-laid stone masonry is arranged upstream of it. There are two drainage galleries embedded in the body of the dam. Located at elevations of 49.50 and 59.00 m, each gallery has a width of 1.5 m (refer to Figure 2). A water transmission pipeline with a diameter of 0.6 m is arranged in the gallery. The leaks in the gallery at 49.50 m are severe, and several leaks have been discovered in the downstream dam toe of the right abutment after investigation (see Figure 3). In September 2020, the daily maximum seepage volume, as per statistical records, was approximately 500 m^3. Furthermore, the reservoir dam has been operational for over 20 years, resulting in the accumulation of a thick layer of silt beneath it.

METHODOLOGY

The FFF method technique

Theory of the FFF method

As described previously, traditional geophysical methods are frequently insufficient for collecting exact data from the concrete dam's surface. Therefore, this section is devoted to presenting the theory of the FFF method deployed at the concrete gravity dam. The leakage pathway in the dam body and dam foundation can be regarded as a porous material (Ray et al., 2012). Under steady-state conditions in the viscous laminar flow regimes, the flow in an isotropic fully water-saturated heterogeneous medium is described by the groundwater flow equation (Ahmed et al., 2019), which is given by

$$-\nabla \cdot \left(\frac{K}{\rho g} \nabla p \right) = Q_S, \quad (1)$$

where K (in m s^{-1}) denotes the hydraulic conductivity, g (9.81 m s^{-2}) denotes the acceleration of the gravity field, ρ (in kg m^{-3}) is the fluid mass density, p (in Pa) is porewater pressure, and Q_S (in s^{-1}) is the hydraulic source or sink term.

When the source/sink term is absent, equation 1 can be written as

$$-\nabla \cdot \left(\frac{K}{\rho g} \nabla p \right) = 0. \tag{2}$$

This partial differential equation can be solved with appropriate boundary conditions. Typically, a Dirichlet's boundary Γ_D, i.e., a prescribed pressure value p_0, is the air-water interface. In addition, a Neumann's boundary Γ_N, $-\mathbf{n}\cdot\nabla p = 0$ is applied at the water dam interface except for the inlet and outlet of the leakage (see Figure 1a), where $\mathbf{n}$ denotes the outward unit vector normal to Γ_N. If the hydraulic conductivity and the mass density are constant, the differential governing equation for the seepage field can be written as

$$\nabla^2 p = 0. \tag{3}$$

This equation shows that the pressure field satisfies the Laplace equation. Once the pressure field has been solved, the Darcy velocity $\mathbf{u}$ is computed with Darcy's law:

$$\mathbf{u} = -\frac{K}{\rho g} \cdot \nabla p. \tag{4}$$

For a steady current field, the current density satisfies Ohm's law (Telford et al., 1990):

$$\mathbf{j} = \sigma \cdot \mathbf{E} = -\sigma \cdot \nabla U, \tag{5}$$

where $\mathbf{j}$ (in A m^{-2}) denotes the current density; σ (in S m^{-1}) is the electrical conductivity; $\mathbf{E}$ (in V m^{-1}) denotes the electrical field; and U (in V) denotes the electric potential.

For an electrical field that is constant over time, the time derivative of the charge density is set to zero within the quasi-static limit, and the current density continuity equation can be written as

$$\nabla \cdot \mathbf{j} = 0. \tag{6}$$

Equation 6 denotes the continuity equation, which shows that the divergence of the current density in a conducting medium at any point of the steady current field other than the source is constantly equal to zero. The current density is therefore conservative in the absence of electrical sources and sinks in the quasistatic limit of the Maxwell equations. At Dirichlet's boundary Γ_D, a prescribed potential value $U_0 = 0$ is imposed. At Neumann's boundary Γ_N, $-\mathbf{n}\cdot(\sigma\ \nabla U) = 0$, where $\mathbf{n}$ denotes the outward unit vector normal to Γ_N.

According to equations 5 and 6, if the conductivity is a constant value, the differential governing equation of the electric potential is as follows:

$$\nabla^2 U = 0. \tag{7}$$

This equation shows that the electric potential satisfies the Laplace equation.

Table 1 outlines the similarities between the current and seepage fields, allowing us to indirectly localize leaks based on shared theory and boundary conditions. When both electrical and hydraulic leakages follow the same paths, using the current field to fit the seepage field aids in leak localization. Measuring the distribution of the transmitted signal's current field effectively identifies leaks, creating a seamless connection between the two fields for detection and identification. During on-site work, we transmit electrical current between electrodes A and B, positioned upstream and downstream, respectively. The resulting electrical potential distribution in the water reservoir is then measured using a probe (Figure 4). Using

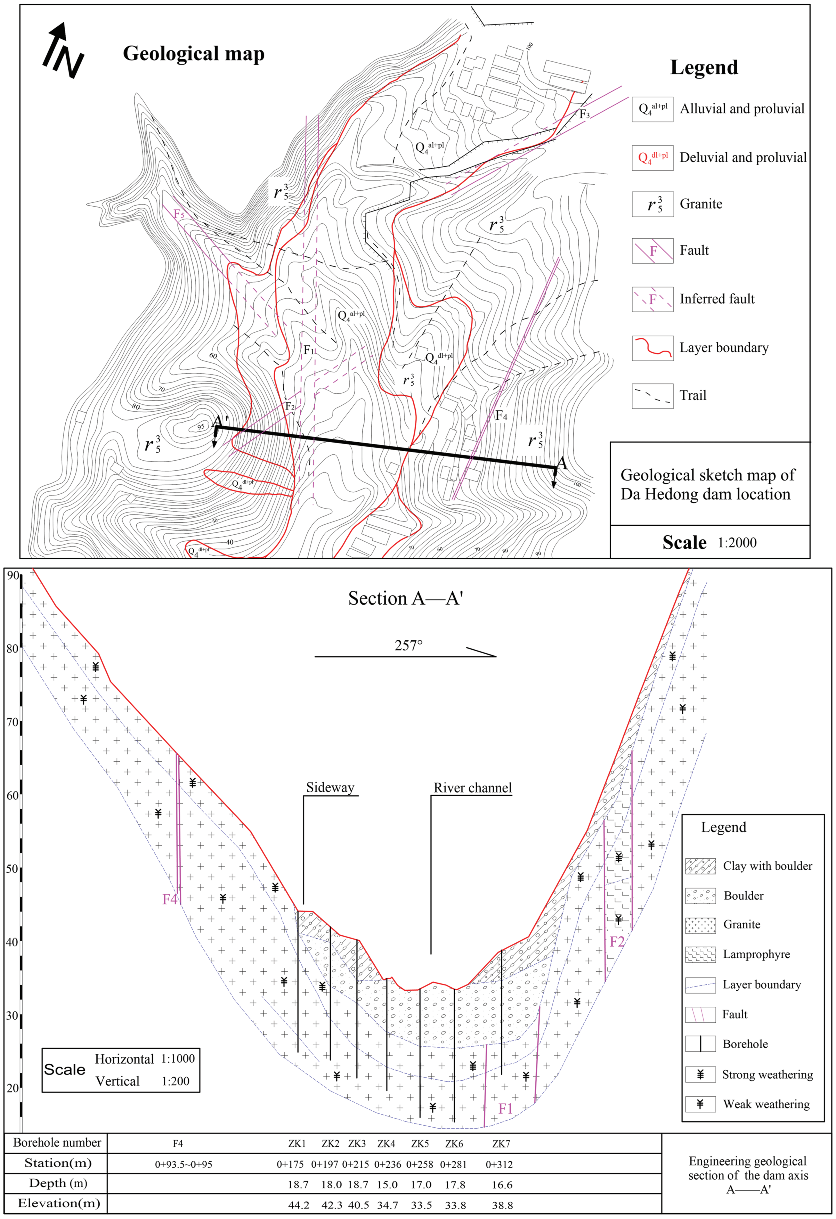

Figure 1. Geologic map of the Da Hedong dam location and related geologic cross section. Q4 represents the quaternary sediment.

the FFF method easily allows access to the leakage inlet, facilitating leak detection and localization.

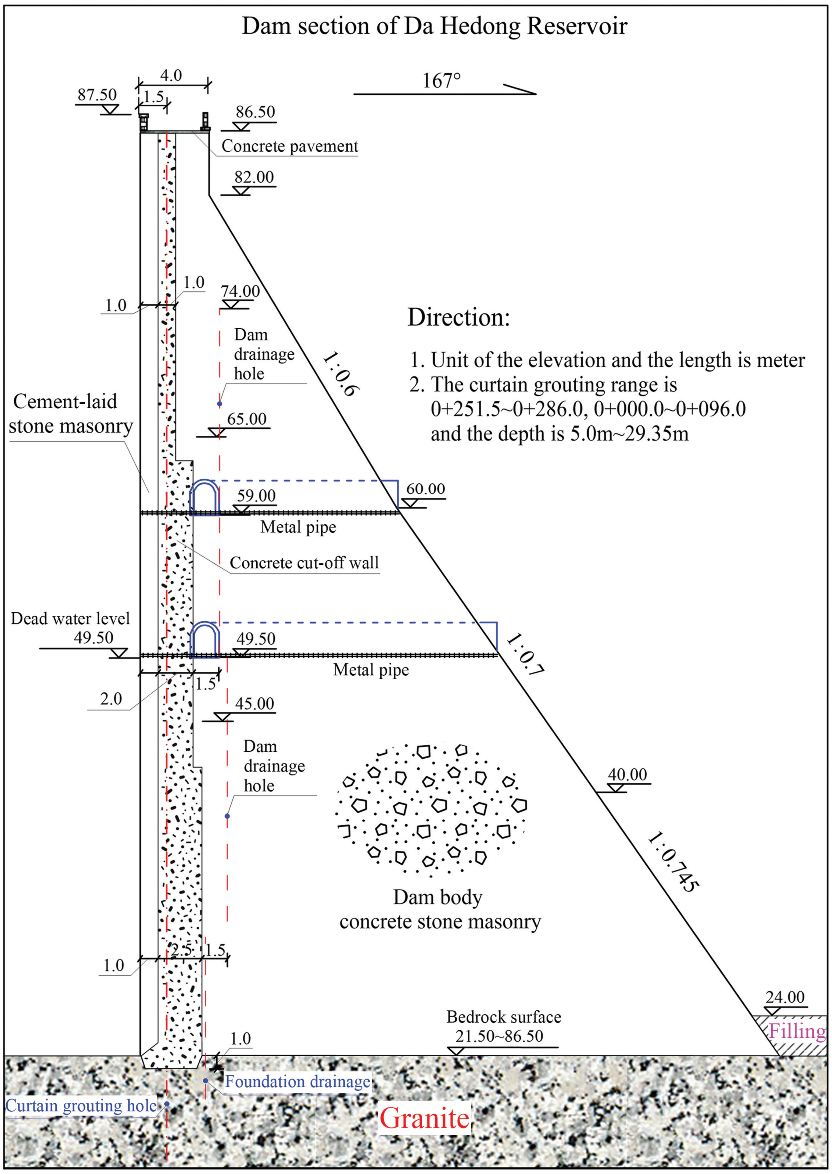

Figure 2. Longitudinal section of the Da Hedong Reservoir dam. The elevation of the base of the reservoir ranges from 21.50 to 86.50 m, and the maximum height difference is 65.0 m. The curtain grouting is implemented in dam sections 0 + 251.5−286.0 and 0 + 0−096.0 during the construction of the dam.

FFF method survey

Figure 5a and 5b shows the potential distribution in a water reservoir with a leak. A point power supply (+) is positioned at O, and the current mainly flows along the subsurface leak path to the reservoir's bottom. The probe in the water body then observes the potential. The potential formula for the observation point M in the water layer, based on the geoelectric model (Telford et al., 1990; Parasnis, 2006; Zheng et al., 2012), is as follows:

$$U = \frac{\mathbf{I}_0(1+m)}{2L}\cdot\frac{\lambda}{2\pi\mathrm{sh}\lambda}\int_0^{2L}\frac{\mathrm{ch}\lambda\left(1-\frac{n}{2L}\right)}{r}dn, \tag{8}$$

$$r = \sqrt{x^2+(z-n)^2}, \tag{9}$$

$$\lambda = 0.932\cdot\frac{2L}{d}\cdot\frac{1}{\sqrt{\frac{\rho_1}{\rho_0}\cdot\lg\left(\frac{2L}{d}\right)}}, \tag{10}$$

where $\mathbf{I}_0$ denotes current intensity at the outlet O, ρ_1 denotes the resistivity of the dam body and dam foundation, ρ_0 denotes the resistivity of the leakage pathway, $2L$ denotes the length of the leakage pathway, d is the radius of long cylindrical conductor (leakage pathway) $m = ((\rho_2-\rho_1)/(\rho_2+\rho_1))$, ρ_2 denotes the resistivity of reservoir water, and $(x\ z)$ denotes the coordinate of observation, n is $0-2L$.

The potential in equation 8 is derived for x and z, respectively; then the gradient equations are obtained along the horizontal x-direction and the vertical z-direction as

$$\left(\frac{\partial U}{\partial x}\right)_S = \frac{\mathbf{I}_0(1+m)\rho_1}{2L}\cdot\frac{\lambda}{2\pi\cdot\mathrm{sh}\lambda}\left(\int_0^{2L}\frac{x\cdot\mathrm{ch}\lambda\left(1-\frac{n}{2L}\right)}{r^3}dn\right), \tag{11}$$

$$\left(\frac{\partial U}{\partial z}\right)_S = \frac{\mathbf{I}_0(1+m)\rho_1}{2L}\cdot\frac{\lambda}{2\pi\cdot\mathrm{sh}\lambda}\left(\int_0^{2L}\frac{(z-n)\cdot\mathrm{ch}\lambda\left(1-\frac{n}{2L}\right)}{r^3}dn\right). \tag{12}$$

Equations 11 and 12 provide theoretical formulas for potential differences in the horizontal and vertical gradient methods, respectively. The measuring electrodes (probe) are positioned at the reservoir's bottom ($z = 2L$). For the horizontal potential gradient, the dipole MN is placed horizontally with a value of zero at $x = 0$, becoming negative for $x < 0$ and positive for $x > 0$. For the vertical potential gradient, the dipole MN is placed vertically, with the largest value at the leakage inlet of the reservoir's bottom — closer inlets yield a higher anomaly value. Figure 5c shows the analytical solution to the potential difference. In the FFF method, placing the probe closer to the leakage inlet enhances resolution. This allows us to detect the distribution of the current field, understand flow-field patterns, ultimately pinpoint leaks and identify the leakage pathway.

We use the DB-3A device, including transmitter, receiver, and probe (He, 2018), for on-site FFF data acquisition. The FFF method identifies leaks by supplying power upstream and downstream of the dam and using a voltmeter (a measuring range of 250 μV–60 mV and an input impedance of 150 kΩ) to retrieve an abnormal electrical signal in the water reservoir. Based on theoretical simulation, we intend to use the vertical potential difference method to detect bottom reservoir leaks and the horizontal potential difference method for dam body leaks. For bottom reservoir detection, the probe is towed by a boat for acquisition per second. We calculate the position of the probe at the reservoir bottom based on the angle and length of the cable inclination. At the upstream face of the dam body, a detection grid space of 2.0 × 1.0 m is established parallel to the dam, facilitated by a designed plastic frame (see Figure 6). Before the survey, two metal pipes are closed to prevent interference with anomalies indicating the real leakage inlet. Data acquisition is performed in two parts: at the upstream face and the reservoir's bottom. GPS is used to maintain the accuracy of the measurement position.

Numerical modeling of the FFF survey

In this section, we aim to validate the efficacy of the FFF method through two synthetic cases, and a reasonable arrangement of on-site surveys and interpretations of data are conducted based on the outcomes of the numerical simulation. The first case illustrates how to effectively detect leaks in the dam body and foundation using the FFF method (horizontal or vertical potential difference approach). To facilitate the supply of domestic and irrigation water to downstream residents, the dam body typically has drainage and water supply pipelines. However, the high conductivity of the metal pipe has a direct impact on the detection results of the FFF method. Hence, it is necessary to eliminate the effect of the metal pipe on the leakage detection results. We roughly eliminate the influence of the metal pipe on the original detection data using the superposition principle to have an approximate response for a qualitative interpretation. In addition, the silt layer beneath the reservoir is characterized by a high coarse particle content in the upper layer and a high fine particle content in the lower layer. Due to the presence of clay minerals, the resistivity of the silt layer is low (Lee et al., 2010; Long et al., 2012). Therefore, the second case is simulated to calculate the response of the FFF method in the presence of the metal pipe and the silt layer.

The numerical simulation problem is solved using COMSOL Multiphysics, which can be used to solve electrical, electrical magnetic, and heat transfer problems (Butler and Sinha, 2012). In our simulation approach, each component of the dam is modeled, including the dam foundation, rock body, leakage pathway, water reservoir, metal pipe, and silt layer. We assign resistivity values of 4000, 3000, 3000, 3000, 200, 40, 1, and 20 Ω m, respectively. For the electric problem, an insulating boundary condition is imposed at the dam/air interface ($\mathbf{n} \cdot \mathbf{j} = 0$). Electric ground boundary conditions $U = 0$ are imposed at the remaining boundaries. To avoid the influence of the boundary conditions on the electric potential distribution, the model's left, right, and bottom are set to infinite-element domains.

GPR survey

A transmitting antenna emits a high-frequency electromagnetic (EM) signal, which travels through the object being measured to investigate the internal structure. The propagation velocity (Basile et al., 2000) is strongly related to the setting of the relative dielectric constant, so it is necessary to determine an appropriate dielectric constant (Hui and Haitao, 2011) in the field using equation 13 as follows:

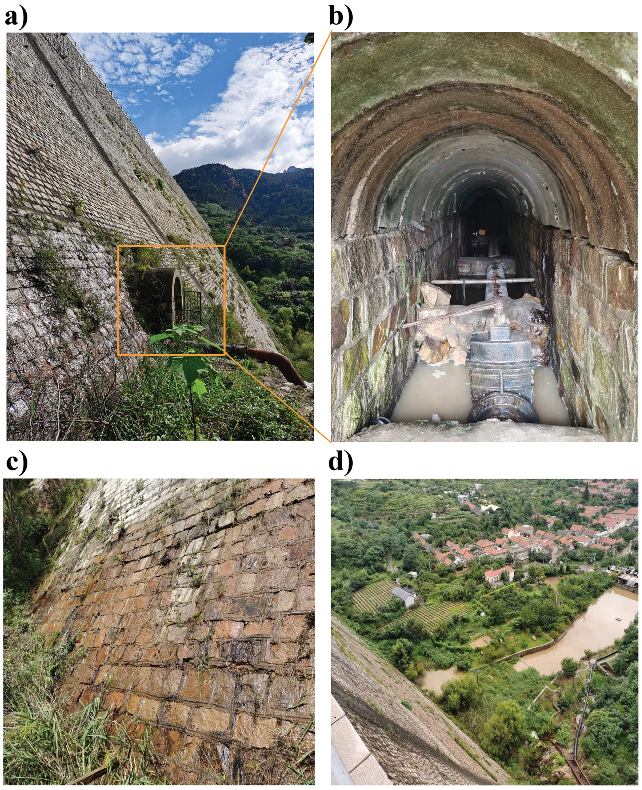

Figure 3. Pictures of dam leakages. (a and b) The water collection gallery and the drainage pipe at an elevation of 49.5 m, (c) free flow of the dam slope near the elevation of 49.5 m downstream at the right abutment, and (d) sump pit at the toe in the middle of the dam.

Table 1. Similarities between the seepage and current fields.

Seepage field	Current field
Darcy's law $\mathbf{u} = -(K/\rho g) \cdot \nabla p$	Ohm's law $\mathbf{j} = -\sigma \cdot \nabla U$
Darcy velocity $\mathbf{u}$	Current density $\mathbf{j}$
Hydraulic conductivity K	Conductivity σ
Governing equation $\nabla^2 p = 0$	Governing equation $\nabla^2 U = 0$
Porewater pressure p	Electric potential U
Neumann's boundary $-\mathbf{n} \cdot \nabla p = 0$	Neumann's boundary $-\mathbf{n} \cdot (\sigma \ \nabla U) = 0$
Dirichlet's boundary $p = p_0$	Dirichlet's boundary $U = 0$

$$v = \frac{2l}{t} = \frac{c}{\sqrt{\varepsilon r}}, \tag{13}$$

where v (in m/s) denotes the velocity of an EM wave in the underground medium, l (in m) is the depth of the observed object, t (in ns) is the two-way traveltime, c (0.3 m/ns) is the propagation velocity of an electromagnetic wave in a vacuum, and ε_r (dimensionless) is the relative dielectric constant of the material.

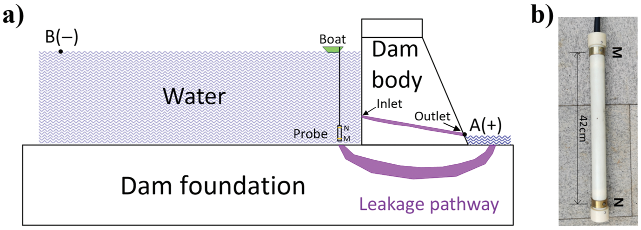

Figure 4. Layout of the electrode array used at the reservoir's bottom. (a) Cross section of the dam and measurement used to detect leakage inlets using the FFF method. The figure shows two types of leaks, one in the dam body itself and the other in its foundations; A and B denote the current electrodes whereas N and M denote the voltage electrodes. (b) A probe with two ring voltage electrodes to measure the potential difference of the transmitted signal electrical field.

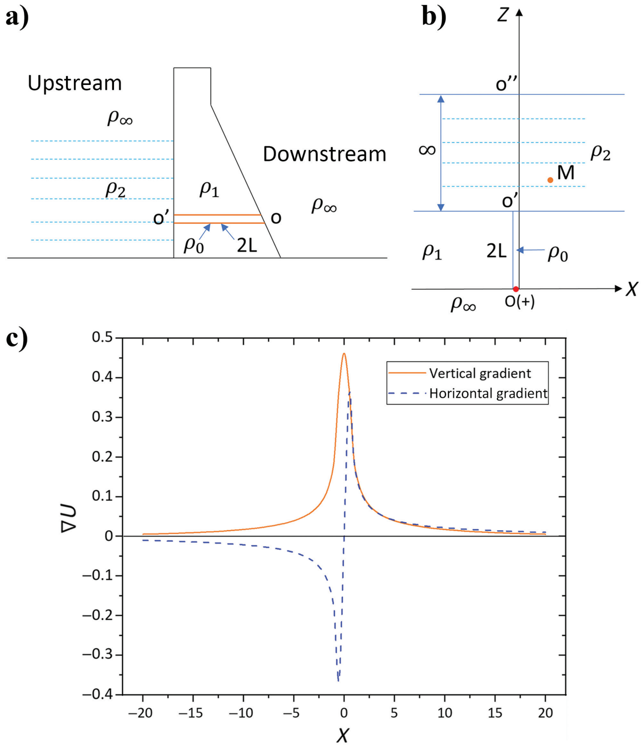

Figure 5. The model with the leakage pathway and analytical solution. (a) Cross section of a dam with a leakage pathway in the dam foundation. (b) Geoelectric model diagram of (a). Here, O denotes the leakage outlet, O′ denotes the leakage inlet, and O–O′ denotes a cylindrical leakage pathway with a length of $2L$. The resistivity of the water, dam foundation, and leakage pathway are written as ρ_2, ρ_1, and ρ_0, respectively. (c) The theoretical results of the horizontal and vertical potential gradients. The parameters used to plot Figure 5c with reference to equations 11 and 12: $\rho_0 = \rho_2 = 40\ \Omega\,\mathrm{m}$, $\rho_1 = 4000\ \Omega\,\mathrm{m}$, $L = 10$ m, $I_0 = 0.5$ A, $z = 20$ m, and $d = 0.5$ m.

The EM waves create reflections at interfaces with different permittivity, and the strength of the reflection is proportional to the permittivity difference across the interface (Prinzio et al., 2010). Therefore, interfaces with larger permittivity (e.g., water with 81, concrete with 4–8) are more easily detected, leading to improved outcomes. In its typical operational mode, a GPR survey is conducted across the surface of the structure. During this process, the antenna system gathers the backscattered field at various points along a scanning line. GPR surveys generate grayscale or colored B-scans, providing radar images for a better understanding of underground structures and anomalies.

Water pressure test

A water pressure test is conducted in situ by injecting high-pressure water into a borehole to measure water loss (Slowik and Saouma, 2000). To carry out this test, one has to isolate a certain length of the borehole using packers and inject pressurized water at a fixed pressure head (e.g., Robinson et al., 2016). The water will penetrate through the cracks in the borehole wall until it reaches a stable seepage value. From the pressure head, the length of the test section, and the final quantity of stable water injected, the permeability of the rock mass can be calculated as

$$q = \frac{Q}{L \cdot p}, \tag{14}$$

where q (in Lu) denotes permeability or Lugeon value, Q (in L/min) denotes the quantity of water injected per minute, L (in m) denotes the length of the test section, and p (in MPa) denotes the water pressure. The water pressure test is conducted to determine whether

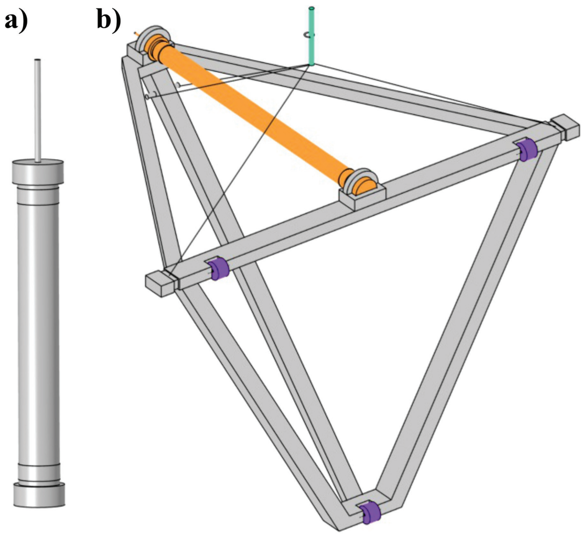

Figure 6. Layout of the DB-3A sensor. (a) The sensor is placed vertically to measure the vertical potential difference at the reservoir's bottom and (b) the probe is fitted to a frame for measuring the horizontal potential difference at the upstream face.

there is any leakage in the cut-off wall and whether the silt layer has an impact on the detection results of the FFF method.

RESULTS

Results from the numerical investigations

Figure 7 shows the geometry of the leakage in the dam body and foundation, along with the current density distribution concentrated at the inlet and pathway. Detecting dam body leaks involves placing the investigation line near the upstream face, using vertical and horizontal potential gradient approaches. Comparing results at different MN electrode spacings (Figure 8a) reveals larger anomalies with increased spacing, indicating a larger leakage inlet. At MN = 0.4 m, the maximum vertical and horizontal potential differences are $V_{\mathrm{MN}} = 0.48$ V and $V_{\mathrm{MN}} = 0.65$ V, respectively. The horizontal gradient method is more effective in detecting leaks at the upstream face. For dam foundation leakage, the investigation line is near the reservoir's bottom, and vertical and horizontal potential gradient approaches are applied. Results at different MN electrode distances (Figure 8b) show maximum vertical and horizontal potential differences of $V_{\mathrm{MN}} = 0.41$ V and $V_{\mathrm{MN}} = 0.37$ V at MN = 0.4 m, respectively. The horizontal potential gradient method has a zero potential difference at the leakage inlet, whereas the vertical potential gradient method has a maximum value, proving more effective at locating leaks at the reservoir's bottom. Numerical results support theoretical interpretation (equations 11 and 12). During on-site work, we use the horizontal gradient approach for dam body leakage and the vertical gradient approach for leakage in the dam foundation and reservoir. In addition, we ensure that the spacing between electrodes is optimized.

In Figure 9a, the dam model with a metal pipe and a silt layer is shown. A 0.6 m diameter metal pipe with 1 Ω m resistivity is added to maintain the other dam components from Figure 7. Figure 9c shows the current density distribution with a metal pipe, showing a significant increase in anomaly compared to the model without it (Figure 9b). Assuming a background value of 0.045 A/m^2, areas above this are considered anomalies, ignoring the two real leakage inlets. Evaluating the impact of a 5 m thick silt layer with a resistivity of 20 Ω m above the dam foundation, Figure 9c and 9d demonstrates its suppressive effect on current density at the leakage inlet. Silts deposited during dam operation create a low permeability sediment layer below the reservoir (Tran et al., 2007), hindering water flow to the leakage pathway, which is crucial in the FFF method. Therefore, a comprehensive evaluation of the detection results, including the small anomalous value at the reservoir's bottom, is necessary.

Numerical simulation results reveal a significant impact of the metal pipe on detection results. The electrical potential follows Laplace's equation, with a linear potential function obeying the superposition principle (Telford et al., 1990). To eliminate the pipe's influence on the original data, we use the principle of current field superposition, comparing simulation data with and without the pipe. Using the model in Figure 9a, simulation outcomes for the potential difference in the presence and absence of the metal pipe (Figure 10) show the pipe's influence up to 6 m. Linear calculations reduce the original data to the condition without metal pipe (which corresponded to the background values), estimated from the original potential difference curve.

FFF results from the field case study

We complete the fieldwork in two days. As shown in Figure 11, electrodes A and B are placed at the downstream leakage outlet and approximately 300 m upstream from the dam. Transmitting a 110 V potential and 500 mA current between electrodes A and B, we use Surfer software for on-site data plotting.

Analyzing the horizontal potential difference data collected from the FFF method at the upstream face, we assume that values 0–40 mV are representing normal areas near the pipe and identify most leakages concentrating in the right abutment of the dam (see Figure 12a). At the reservoir's bottom, near the dam body, six potentially anomalous areas are detected (Figure 12b). The conductivity of the dam is complicated; we use a linear calculation to roughly eliminate the metal pipe's interference. We apply the superposition principle in our 3D model (not shown here), simplifying the data by setting the background value to zero potential difference (Figure 12c). This reveals additional anomalies near and around the metal pipes, indicating multiple leaks. Leaks located at the junction between the dam and its foundation may be related to the faults 1 and 2 of the reservoir (Figure 13a), as well as the high-permeability granite present at the dam foundation. Alternatively, they could be linked to the water circulation within the coarse sand and clay layers present at the reservoir bottom. Subsequent water pressure tests will validate our analysis. FFF data for the reservoir's bottom, analyzed for vertical potential difference, identify six areas with anomalies

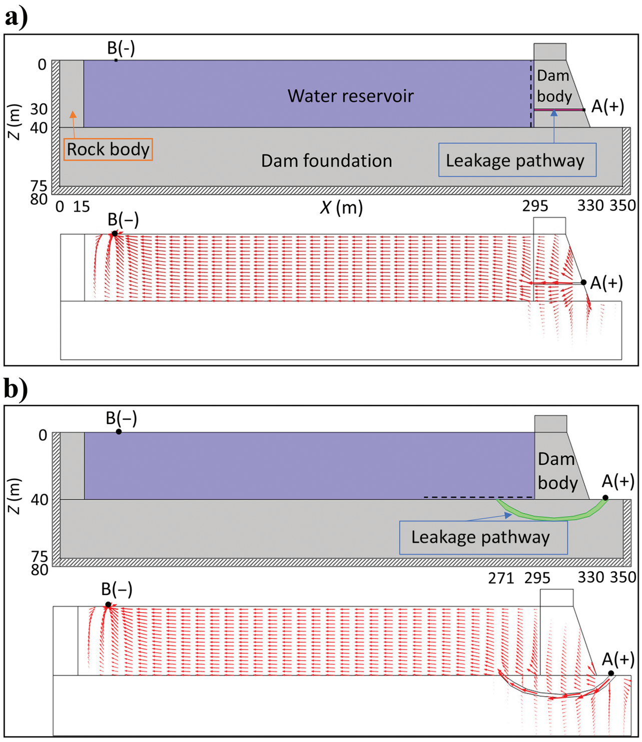

Figure 7. Geometry of the dam body and foundation leakage. (a) Dam model 1: the shaded portion represents the infinite-element domains. Electrode A (+) is located downstream at the leakage outlet, and electrode B (−) is upstream. (b) Dam model 2: the red arrows indicate the current density, which is the maximum at the leakage pathway.

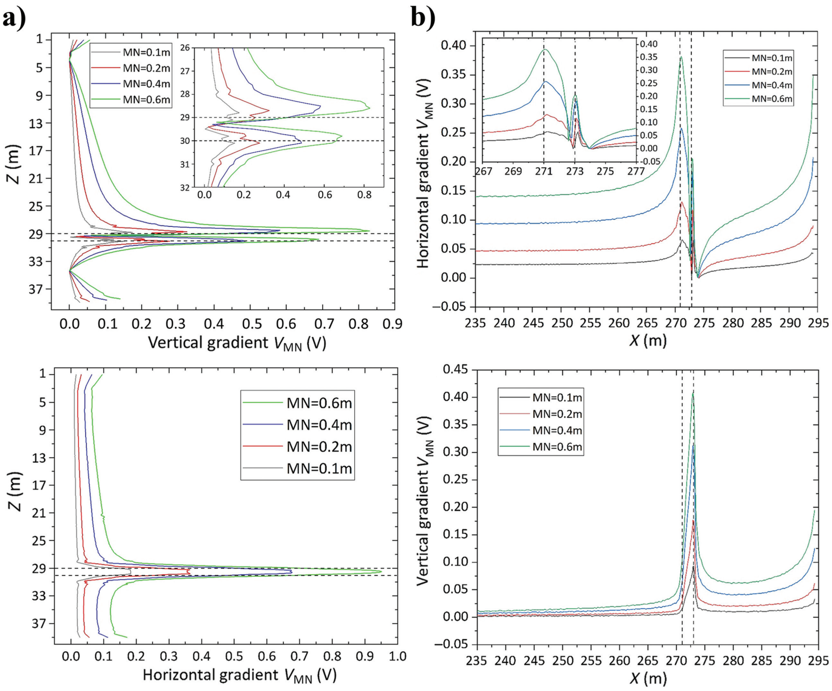

Figure 8. The results of the simulations. (a) The potential difference, including the absolute values of the vertical and horizontal gradients, is measured by a probe located at X = 294.9 m along the measurement line illustrated as the dotted black line in Figure 7a. (b) A probe located at Z = 39.9 m along the measuring line depicted as the dotted black line in Figure 7b measures the potential difference, which includes the absolute values of the vertical and horizontal gradients. The dotted black line indicates the location of the leakage inlet. MN represents the distance between electrodes M and N on the probe.

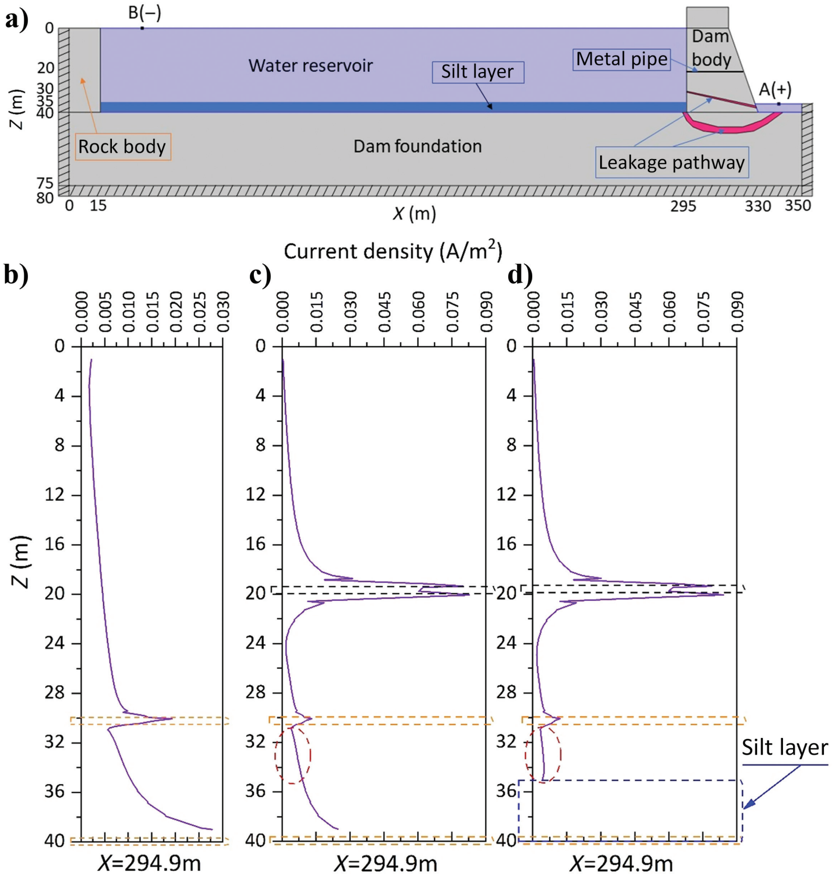

Figure 9. Numerical simulation results of a metal pipe and a silt layer. (a) The geometry of the dam model, (b) current density distribution at X = 249.9 m, without the metal pipe in the dam body and without the silt layer in the reservoir's bottom, (c) current density distribution with the metal pipe and no silt layer at X = 249.9 m, and (d) current density distribution with a metal pipe and a silt layer at X = 249.9 m. The red oval-shaped dashed line indicates the shift in the current density caused by the silt layer. The dotted orange lines at Z = 30 m and Z = 40 m indicate the leakage inlets.

primarily near the right abutment and right shoulder of the water reservoir (Figure 13b). The anomalies may be associated with faults 1 and 2, which contain more conductive veins of lamprophyre. Based on the fault locations indicated in Figure 13a and the morphology of these anomalies, we infer that most of these anomalies are likely related to the faults present at the reservoir bottom. The 10 m thick silt layer (calculated by Figures 2 and 12) below the reservoir contributes to varying degrees of leakage in the dam foundation (see Figure 13c). Fortunately, fault 4 is located at a higher elevation with a narrower fault and no leakage, further suggesting it does not affect the water leakage of the dam.

The collected 3D FFF data for the vertical potential difference at the upstream face confirm the theory of the FFF. The analysis shows the greatest potential difference closest to the upstream face and the smallest furthest away (see Figure 14), validating the FFF method theory (see Figure 14f). This supports the reliability and accuracy of the FFF method in detecting water leakage in concrete dams.

Results from the GPR survey

Based on the location of the dam in the field, the measurements are taken using the SIR 2000 Radar System with a 400 MHz high-frequency antenna (due to issues with the instrument itself, the 100 MHz antenna cannot be used). GPR work is only performed downstream of the right dam abutment due to the concrete masonry slab downstream of the dam, as shown in Figures 2 and 15a, numbered from T_0 to T_5. Onsite, we use equation 13 to calculate the dielectric constant of a dam body with known depth or thickness and then apply this value (approximately 4.0) to the actual dam body measurement. GPR data are collected monostatically with 512 samples, a 100 ns range, and 50 scans per meter. The detection direction is vertical and upward. Processing of the field-collected data is performed using RADAN (GSSI), involving the main steps of distance normalization, surface location determination, filtering, and time-to-depth conversion.

The final profiles are shown in Figure 15b–15g. Line T_0 is located on the gallery's east side at an elevation of 49.5 m, with a length of 10.0 m and a sounding of 7.5 m. The obtained image is shown in Figure 15g. The radar image shows two anomalies that are thought to be caused by small-scale masonry cracks in water-rich areas within the dam body. Other parts of the dam's body are in good condition. Lines T_1 and T_3 are located west of the gallery at an elevation of 49.5 m, with lengths of 10.0, 11.0, and 12.0 m and a sounding of 7.5 m, respectively. The images are obtained and depicted in Figure 15d–15f. Scanning profile T_1 reveals three anomalies, which are interpreted as being caused by small-scale masonry cracks in water-rich areas within the dam body. Scanning profiles T_2–T_3 display four anomalies with strong radar reflections, especially T_3, which may be caused by large-scale cracks of masonry in water-rich areas within the dam body. The radar scanning in Figure 15c shows a slight anomaly, and Figure 15b shows the dam body is in good

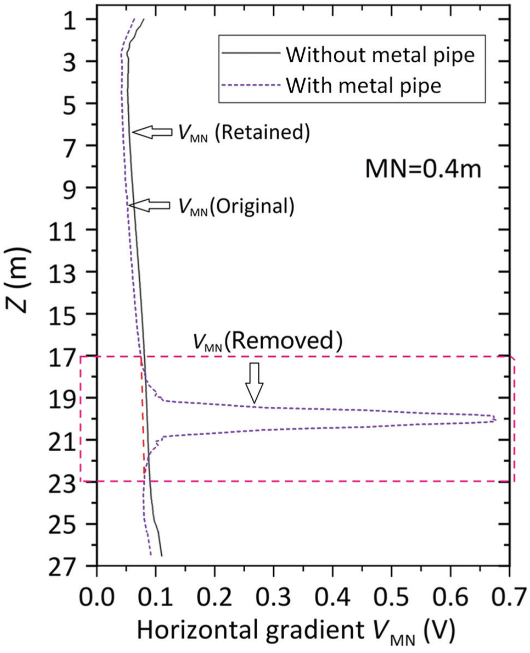

Figure 10. Diagram of the results of removing the effects of the metal pipe. The dashed red line indicates the background value. Here, V_{MN} (original) denotes the real potential difference in the presence of the metal pipe, V_{MN} (retained) denotes the background value in the absence of the metal pipe, and V_{MN} (removed) denotes the value of the removed potential difference using the principle of current field superposition.

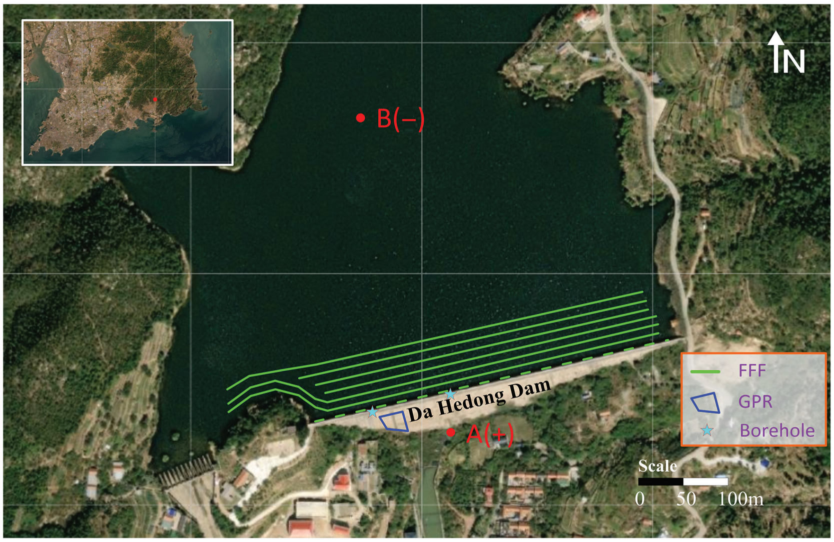

Figure 11. Google Earth view of Da Hedong dam and location of the FFF field investigations and GPR and water pressure test surveys. Electrode A (+) is placed at the leakage outlet downstream, and B (−) is placed upstream, far away from the dam body. The green dashed line and continuous lines depict the trajectory of the boat for the survey at the upstream face and the bottom of the reservoir, respectively. The two boreholes are located at 250 and 348 m, respectively. The measuring lines in the reservoir run from east to west, with an approximate spacing of 5 m between each line. A total of 10 measuring lines have been arranged.

condition and well structured, with no significant anomalies found within a 7.5 m detection distance. The GPR survey results show leakages around the downstream gallery at 49.5 m elevation. We infer that the reservoir water enters the gallery through leaks near the upstream pipe. The flow of water creates voids in the concrete stone masonry, leading to a higher water content.

Results from the water pressure test

Based on the results of the FFF investigations and numerical modeling, we decided to conduct two water pressure tests at the dam crest boreholes (borehole 1 is located at station 250 m and borehole 2 at 348 m). According to equation 14, the result of the test is shown in Table 2. Borehole 1 exhibits a higher absorption rate at the dam foundation, indicating significant leakage issues. Similarly, borehole 2 also shows leakages at the dam foundation. In addition, the results show an encouraging finding: the concrete cut-off wall is nearly intact and has no leakages, and the presence of the silt layer interferes with the detection of the FFF method. The findings suggest that faults and highly permeable rock contribute to leakage problems at the dam foundation.

DISCUSSION

To investigate leakage inlets on the upstream face of the dam further, we should use a smaller detection grid, such as 1.0 m × 0.5 m. However, it means we need to take many measurements to have a decent resolution. In future research, we will develop multichannel devices that can greatly reduce the time needed to accomplish data acquisition. In addition, when implementing the FFF method, it is necessary to know in advance whether there are pipes in the dam. Moreover, when a thick layer of silt exists below the reservoir, the lower potential difference values observed should not be overlooked and might indicate a possible leakage source. We directly use Surfer software to plot the data collected onsite without conducting corresponding 2D or 3D inversion work. In future research, we will conduct in-depth investigations specifically focused on the inversion of the FFF method.

We can easily access the leakage inlet and locate the leaks using the FFF approach. The approximate location information of the leakage pathway can be obtained when we know where the leak starts or ends. The FFF method qualitatively assesses the severity of leakage based on the magnitude of the potential difference. However, the estimated leakage quantities could not be justified by the potential anomalies that resulted from the survey. The future necessitates the quantitative estimation of leakage by integrating alternative approaches.

Considering the upcoming rainy season and to prevent potential interruptions in downstream water supply, we conduct a survey using the FFF method within a limited two-day timeframe. As a result, we do not perform an actual data comparison between the two detection methods of the FFF in this particular instance. A more comprehensive comparison will be conducted in future engineering projects.

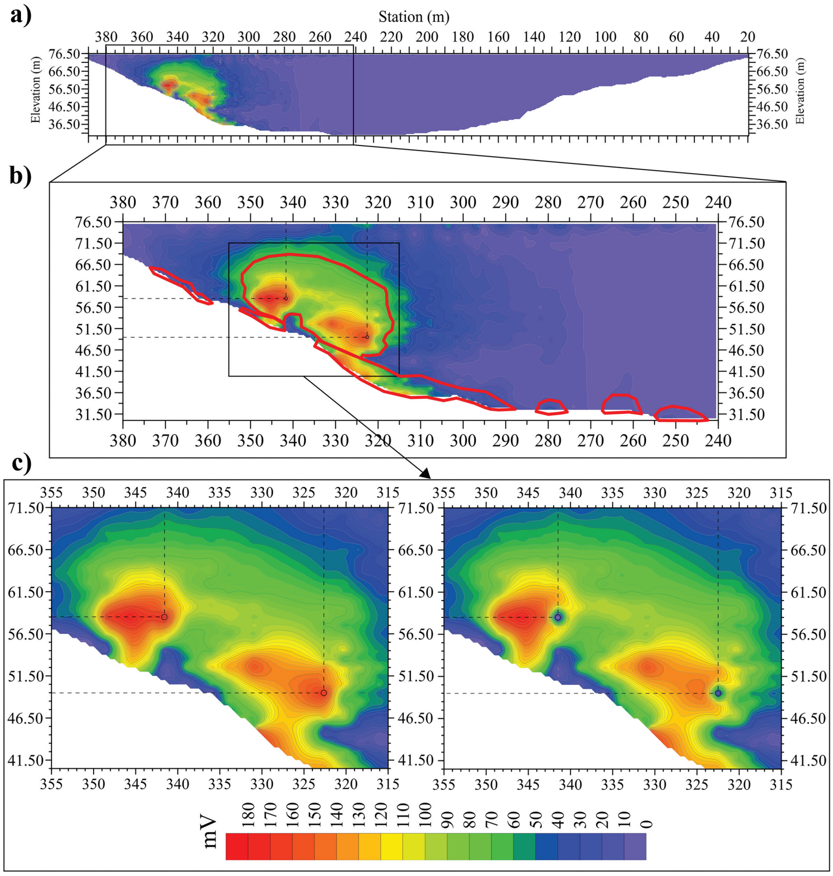

Figure 12. Detection results of the horizontal potential difference at the upstream face. (a) The results of the overall measurement of the upstream face and (b) potential leakage areas are marked with red lines, and metal pipes at elevations of 49.5 and 59.0 m have been marked with two black circles. There are several leakages at the dam's bottom (the station is 245–265 m, 275–285 m, 290–335 m, 345–355 m, and 360–375 m), and these leakage areas have a lower potential difference and should not be ignored. (c) Comparison diagram after the presence (left) and removal (right) of metal pipes.

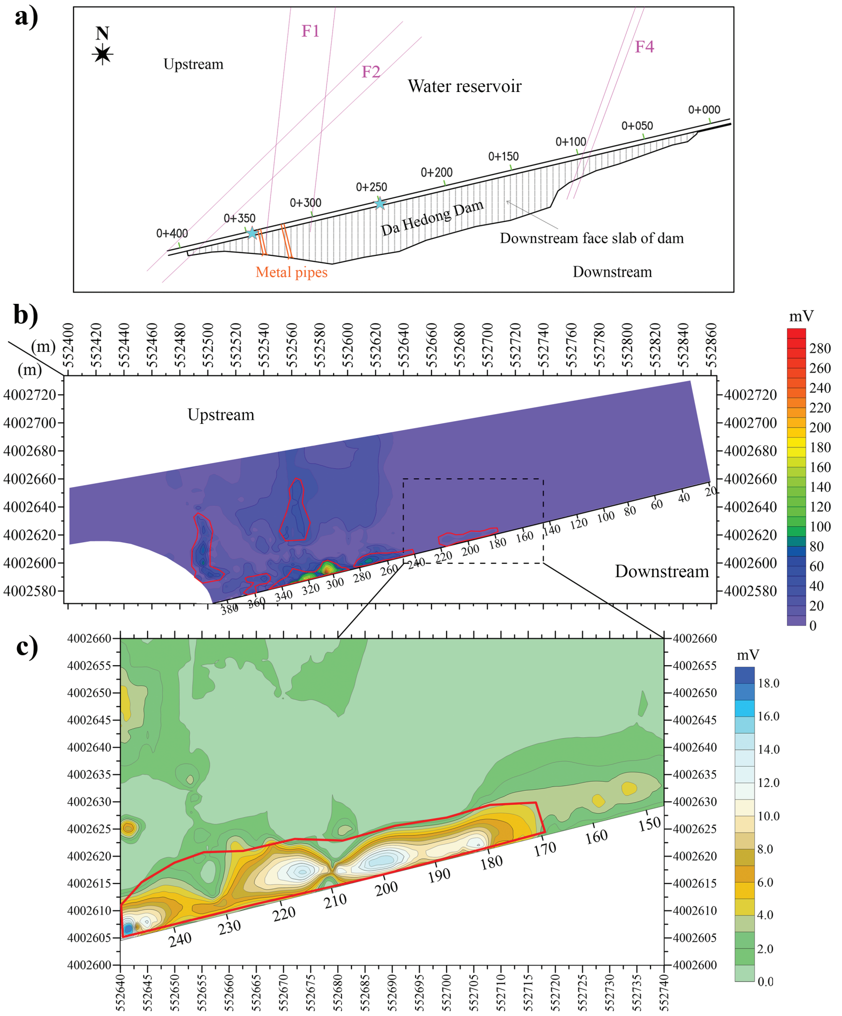

Figure 13. Detection results of the vertical potential difference at the reservoir's bottom. (a) Schematic diagram of the top view of the dam based on geologic settings and dam descriptions. (b) The distribution of the vertical potential difference. Six potential leakage areas are marked with red lines. (c) Potential difference distribution associated with dam foundation leakage in the middle of the reservoir dam.

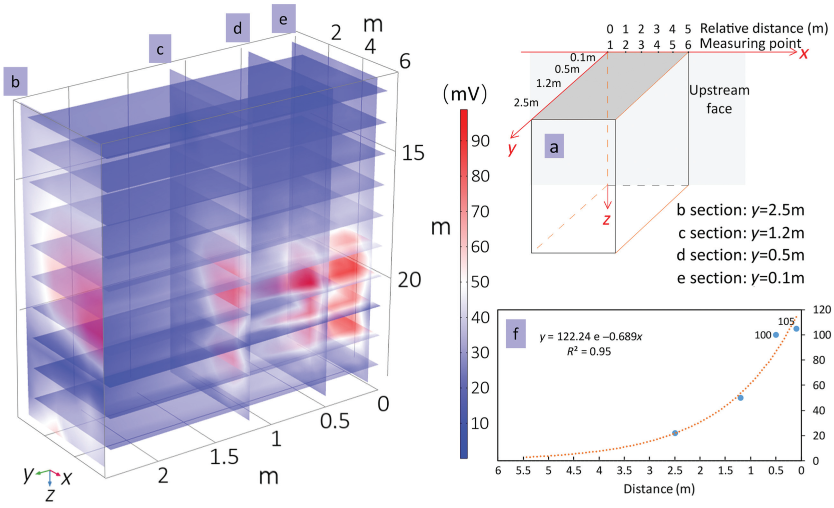

Figure 14. The 3D profiles of the vertical potential difference between the approximate stations at 332 and 337 m, wherein (a) represents the layout diagram, (b–e) represent contour maps of the potential difference at the *XZ* section, and (f) represents vertical potential difference versus distance for the field data ($R^2 = 0.95$). The data points are the maximum observed values in the four profiles, respectively.

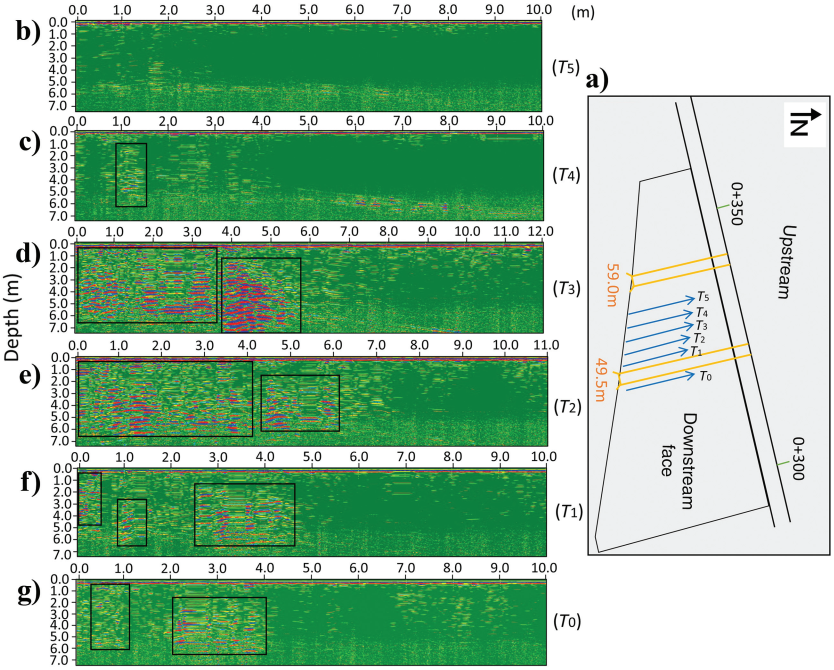

Figure 15. GPR scanning results. (a) Schematic diagram of measuring lines. The pipes at elevations of 59.0 and 49.5 m have been marked (the orange lines), and the relative positions of the six survey lines are shown in blue lines. The detection direction is vertical and upward. (b–g). Depth radar profiles. The black boxes denote potential water-rich areas or void areas caused by differences in dielectric constants, which result in stronger electromagnetic wave reflections. These areas indicate the presence of anomalies within the dam body and can be interpreted as water from the reservoir leaking downstream through a crack near the inlet of the metal pipe at the upstream face (leakage inlets).

CONCLUSION

Theoretical studies, numerical simulations, and field applications show the reliability of the FFF method in detecting leaks within the concrete gravity dam. The results of the FFF are tested against supporting evidence from GPR and water pressure tests. The horizontal gradient method proves most effective for identifying dam body leakage, whereas the vertical gradient method excels in detecting leaks at the reservoir's bottom. Notably, a specially designed plastic frame facilitates horizontal gradient measurements, enabling a comprehensive investigation of the entire dam section by combining both detection techniques.

It is imperative to acknowledge the influential role of the metal pipe within the dam body on FFF method detection outcomes. Consequently, meticulous attention must be given to avoiding the impact of the metal pipe during data processing and analysis. In addition, the presence of a silt layer beneath the reservoir results in a diminished response to the potential difference.

Upon concluding the data analysis, the identified leakages could be attributed to three primary factors. (1) The existence of multiple faults beneath the dam leads to leaks at the contact where the fault meets the dam body. (2) Because the metal pipelines had been previously in use for an extended period, cement-laid stone masonry present around two pipes might become loosened, resulting in water ingress into the gallery

Table 2. Results of the water pressure test in the borehole.

				Hydraulic conductivity	
Borehole/Station	Depth (m)	Elevation (m)	Lithology	Lugeon	cm/s
Borehole 1/250 m	1.0–20.0	85.5–66.5	Concrete cut-off wall	0.33	0.43E−5
	20.0–40.0	66.5–46.5	Concrete cut-off wall	0.23	0.30E−5
	40.0–56.0	46.5–30.5	Concrete cut-off wall	0.11	0.14E−5
	56.0–58.5	30.5–28.0	Strong weathering granite	>100	>1.30E−3
	58.5–63.5	28.0–23.0	Strong weathering granite	>100	>1.30E−3
	63.5–67.0	23.0–19.5	Strong weathering granite	>100	>1.30E−3
	67.0–72.0	19.5–14.5	Strong weathering granite	18.27	2.38E-4
	72.0–80.0	14.5–6.5	Moderate weathering granite	9.54	1.24E-4
Borehole 2/348 m	1.0–11.0	85.5–75.5	Concrete cut-off wall	0.86	1.12E−5
	11.0–20.0	75.5–66.5	Concrete cut-off wall	0.51	0.66E−5
	20.0–23.0	66.5–63.5	Moderate weathering granite	7.11	9.24E−5
	23.0–30.0	63.5–56.5	Moderate weathering granite	5.32	6.92E−5
	30.0–37.0	56.5–49.5	Moderate weathering granite	2.90	3.77E−5
	37.0–43.0	49.5–43.5	Weak weathering granite	0.58	0.75E−5
	43.0–52.0	43.5–34.5	Weak weathering granite	0.41	0.53E−5

Note: The positions of the two boreholes are located at the top of the dam for the location of the concrete cut-off wall, with stations of 250 and 348 m, respectively. Boreholes are drilled vertically downward from the dam crest to a depth of approximately 30 m into the rock mass. 1 Lu ≈ 1.3E−5 cm/s.

and walls through pores. (3) Hydrostatic or dynamic water pressure exerted by the reservoirs could cause leaks in the middle of the dam's foundation. Consideration of these factors establishes a foundation for future seepage healing treatments, promising a substantial reduction in engineering costs.

ACKNOWLEDGMENTS

We appreciate the support provided by the National Natural Science Foundation of China (41674113). X. Zhao thanks the China Scholarship Council (202106710036) for its support. A. Revil is funded by the INTEREG project RITA. We thank Assistant Editor Y. Liu and four anonymous referees for their helpful comments on our manuscript.

DATA AND MATERIALS AVAILABILITY

Data associated with this research are available and can be obtained by contacting the corresponding author.

REFERENCES

Abdulsamad, F., A. Revil, A. Soueid Ahmed, A. Coperey, M. Karaoulis, S. Nicaise, and L. Peyras, 2019, Induced polarization tomography applied to the detection and the monitoring of leaks in embankments: Engineering Geology, **254**, 89–101, doi: 10.1016/j.enggeo.2019.04.001.

Ahmed, A. S., A. Revil, B. Steck, C. Vergniault, A. Jardani, and G. Vinceslas, 2019, Self-potential signals associated with localized leaks in embankment dams and dikes. Engineering Geology, **253**, 229–239, doi: 10.1016/j.enggeo.2019.03.019.

Basile, V., M. T. Carrozzo, S. Negri, L. Nuzzo, T. Quarta, and A. V. Villani, 2000, A ground-penetrating radar survey for archaeological investigations in an urban area (Lecce, Italy): Journal of Applied Geophysics, **44**, 15–32, doi: 10.1016/S0926-9851(99)00070-1.

Butler, S., and G. Sinha, 2012, Forward modeling of applied geophysics methods using Comsol and comparison with analytical and laboratory analog models: Computers and Geosciences, **42**, 168–176, doi: 10.1016/j.cageo.2011.08.022.

Cardarelli, E., M. Cercato, and G. De Donno, 2014, Characterization of an earth-filled dam through the combined use of electrical resistivity tomography, P- and SH-wave seismic tomography and surface wave data: Journal of Applied Geophysics, **106**, 87–95, doi: 10.1016/j.jappgeo.2014.04.007.

Cho, I.-K., and J. Y. Yeom, 2007, Crossline resistivity tomography for the delineation of anomalous seepage pathways in an embankment dam: Geophysics, **72**, no. 2, G31–G38, doi: 10.1190/1.2435200.

COMSOL Multiphysics User's Guide, 2017, Version 5.3: COMSOL AB.

Dai, Q., F. Lin, X. Wang, D. Feng, and R. C. Bayless, 2017, Detection of concrete dam leakage using an integrated geophysical technique based on flow-field fitting method: Journal of Applied Geophysics, **140**, 168–176, doi: 10.1016/j.jappgeo.2017.03.013.

Ferdos, F., B. Dargahi, and L. Solari, 2018, Mechanism of suffusion erosion phenomenon in porous media: Journal of Geology Geoscience, **2**, 2018.

Foster, M., R. Fell, and M. Spannagle, 2011, Statistics of embankment dam failures and accidents: Canadian Geotechnical Journal, **37**, 1000–1024, doi: 10.1139/t00-030.

Guo, Y., Y.-A. Cui, J. Xie, Y. Luo, P. Zhang, H. Liu, and J. Liu, 2022, Seepage detection in earth-filled dam from self-potential and electrical resistivity tomography: Engineering Geology, **306**, 106750, doi: 10.1016/j.enggeo.2022.106750.

Gutierrez, F., M. Mozafari, D. Carbonel, R. Gómez, and E. Raeisi, 2015, Leakage problems in dams built on evaporites. The case of La Loteta Dam (NE Spain), a reservoir in a large karstic depression generated by interstratal salt dissolution: Engineering Geology, **185**, 139–154, doi:10.1016/j.enggeo.2014.12.009.

Haas, A., A. Revil, M. Karaoulis, L. Frash, J. Hampton, M. Gutierrez, and M. Mooney, 2013, Electric potential source localization reveals a borehole leak during hydraulic fracturing: Geophysics, **78**, no. 2, D93–D113, doi: 10.1190/geo2012-0388.1.

He, J., 2018, Combined application of wide-field electromagnetic method and flow field fitting method for high-resolution exploration: A case study of the Anjialing No.1 coal mine: Engineering, **4**, 667–675, doi: 10.1016/j.eng.2018.09.006.

Huang, Y., X. Hou, Z. Fu, and J. Wang, 2018, Detection of leakage paths at the Wanyao dam body in Southwest China by hydrochemical analysis and tracer testing: Environment Earth Science, **77**, 1–13, doi: 10.1007/s12665-018-7981-6.

Hui, L., and M. Haitao, 2011, Application of ground penetrating radar in dam body detection: Procedia Engineering, **26**, 1820–1826, doi: 10.1016/j.proeng.2011.11.2372.

Ikard, S. J., J. Rittgers, A. Revil, and M. A. Mooney, 2015, Geophysical investigation of seepage beneath an earthen dam: Ground Water, **53**, 238–250, doi: 10.1111/gwat.12185.

Jessop, M., A. Jardani, A. Revil, and V. Kofoed, 2018, Magnetometric resistivity: A new approach and its application to the detection of preferential flow paths in mine waste rock dumps: Geophysical Journal International, **215**, 222–239, doi: 10.1093/gji/ggy275.

Ketola, M., 1972, Some points of view concerning Mise-à-la-Masse measurements: Geoexploration, **10**, 1–21, doi: 10.1016/0016-7142(72)90010-5.

Kumar, D., N. S. Krishnamurthy, S. Ahmed, S. Jain, and R. Dhar, 2003, Mise-à-la-Masse technique in establishing the lateral extension of fractures in hard rocks: Journal of the Geological Society of India, **61**, 185–194.

Lee, J. Y., J. C. Santamarina, and C. Ruppel, 2010, Parametric study of the physical properties of hydrate-bearing sand, silt, and clay sediments: 1. Electromagnetic properties: Journal of Geophysical Research, **115**, B11104, doi: 10.1029/2009JB006669.

Ling, C., A. Revil, F. Abdulsamad, Y. Qi, A. Soueid Ahmed, P. Shi, S. Nicaise, and L. Peyras, 2019a, Leakage detection of water reservoirs using a Mise-à-la-Masse approach: Journal of Hydrology, **572**, 51–65, doi: 10.1016/j.jhydrol.2019.02.046.

Ling, C., A. Revil, Y. Qi, F. Abdulsamad, P. Shi, S. Nicaise, and L. Peyras, 2019b, Application of the mise-à-la-masse method to detect the bottom leakage of water reservoirs: Engineering Geology, **261**, 105272–15, doi: 10.1016/j.enggeo.2019.105272.

Long, M., S. Donohue, J.-S. L'Heureux, I.-L. Solberg, J. S. Rønning, R. Limacher, P. O'Connor, G. Sauvin, M. Rømoen, and I. Lecomte, 2012, Relationship between electrical resistivity and basic geotechnical parameters for marine clays: Canadian Geotechnical Journal, **49**, 1158–1168, doi: 10.1139/t2012-080.

Mansinha, L., and C. J. Mwenifumbo, 1983, A mise-à-la-masse study of the Cavendish geophysical test site: Geophysics, **48**, 1252–1257, doi: 10.1190/1.1441548.

Meng, Y., Y. Fang, M. Wan, Q. Su, B. Tian, and F. Tong, 2019, Research of concrete dam leakage detection based on anomaly current field of reservoir water: Journal of Applied Geophysics, **160**, 242–253, doi: 10.1016/j.jappgeo.2018.11.016.

Nan, S., J. Ren, F. Ni, L. Zhang, and X. He, 2022, Heat tracing of embankment dam leakage: Laboratory experiments and 2D numerical modelling: Journal of Hydrology, **608**, 127663, doi: 10.1016/j.jhydrol.2022.127663.

Parasnis, D., 2006, Three-dimensional electric mise-à-la-masse survey of an irregular lead-zinc-copper deposit in central Sweden: Geophysical Prospecting, **15**, 407–437, doi: 10.1111/j.1365-2478.1967.tb01796.x.

Peyras, L., P. Royet, L. Deroo, R. Albert, J.-P. Becue, S. Aigouy, E. Bourdarot, D. Loudiere, and J.-B. Kovarik, 2011, French recommendations for limit-state analytical review of gravity dam stability: European Journal of Environmental and Civil Engineering, **12**, 1137–1164, doi: 10.1080/19648189.2008.9693071.

Prinzio, M. D., M. Bittelli, A. Castellarin, and P. R. Pisa, 2010. Application of GPR to the monitoring of river embankments: Journal of Applied Geophysics, **71**, 53–61, doi: 10.1016/j.jappgeo.2010.04.002.

Ray, N., T. van Noorden, F. Frank, and P. Knabner, 2012, Multiscale modeling of colloid and fluid dynamics in porous media including an evolving microstructure: Transport in Porous Media, **95**, 669–696, doi: 10.1007/s11242-012-0068-z.

Robert, T., D. Caterina, J. Deceuster, F. Olivier, and F. Nguyen, 2012, A salt tracer test monitored with surface ERT to detect preferential flow and transport paths in fractured/karstified limestones: Geophysics. **77**, no. 2, B55–B67, doi: 10.1190/geo2011-0313.1.

Robinson, J., L. Slater, T. Johnson, A. Shapiro, C. Tiedeman, D. Ntarlagiannis, C. Johnson, F. Day-Lewis, P. Lacombe, T. Imbrigiotta, and J. Lane, 2016, Imaging pathways in fractured rock using three-dimensional electrical resistivity tomography: Ground Water, **54**, 186–201, doi: 10.1111/gwat.12356.

Sjödahl, P., T. Dahlin, and B. Zhou, 2006, 2.5D resistivity modeling of embankment dams to assess influence from geometry and material properties: Geophysics, **71**, no. 3, G107–G114, doi: 10.1190/1.2198217.

Slob, E., M. Sato, and G. Olhoeft, 2010, Surface and borehole ground-penetrating-radar developments: Geophysics, **75**, no. 5, 75A103–75A120, doi: 10.1190/1.3480619.

Slowik, V., and V. E. Saouma, 2000, Water pressure in propagating concrete cracks: Journal of Structural Engineering, **126**, 235–242, doi: 10.1061/(ASCE)0733-9445(2000)126:2(235).

Telford, W. M. N., L. Geldart, and R. Sheriff, 1990, Applied geophysics: Cambridge University Press.

Tingzhe, H., P. Li, Q. Duan, L. Zhang, and J. Shi, 2013, Development of foundation pit leakage detector based on flow-field fitting method: IEEE International Conference of IEEE Region 10.

Tran, M. N., M. F. Randolph, and D. W. Airey, 2007, Installation of suction caissons in sand with silt layers: Journal of Geotechnical and Geoenvironmental Engineering, **133**, 1183–1191, doi: 10.1061/(ASCE)1090-0241(2007)133:10(1183).

Zeidan, B. A. 2015, Design and analysis of concrete gravity dams: Tanta University.

Zhang, L., Y. Xu, and J. S. Jia, 2009, Analysis of earth dam failures: A database approach: Georisk Assessment and Management of Risk for Engineered Systems and Geohazards, **3**, 184–189, doi: 10.1080/17499510902831759.

Zhao, X., H. Zhang, K. Wei, P. Wang, Q. Ren, and D. Zhang, 2021, Flow field fitting method and acoustic Doppler velocity measurement: A new approach for detecting leakage pathways in concrete-face rockfill dams: Earth and Space Science, **8**, 1–17, doi: 10.1029/2021EA001875.

Zhao, X., H. Zhang, P. Wang, Q. Ren, D. Zhang, L. Yan, and X. Zhu, 2023, Flow-field fitting method applied to the detection of leakages in the concrete gravity dam: Journal of Applied Geophysics, **208**, 104896, doi: 10.1016/j.jappgeo.2022.104896.

Zheng, C., H. Wang, and M. Zheng, 2012, Comments on flow field method: Progress in Geophysics, **27**, 2190–2197.

Biographies and photographs of the authors are not available.